

Observation of Higher-Mode Rayleigh Waves from Ambient Noise in the Tarim Basin, China

Tongtong Xie^{1,2}, Tao Xu^{*3,4}, Yingjie Yang⁵, Xiaobo Tian^{1,4}, Jiyun Lin⁶, Chenglong Wu^{3,4}, and Zhanwu Lu⁷

Abstract

Higher mode surface waves, which can provide additional constraints on subsurface structures in addition to fundamental modes in surface-wave tomography, have been observed from ambient noise cross-correlation functions (CCFs) in sedimentary basins in oceans or near coastlines. However, few studies show that higher mode surface waves can be observed and extracted directly from ambient noise CCFs in inland basins. In this study, we report observations of high signal-to-noise ratio fundamental and the first higher mode Rayleigh waves at a period range of 0.2–1.90 s and 0.2–1.35 s, respectively, from ambient noise CCFs in the southeastern margin of the Tarim basin, the biggest inland basin in China. We confirm the credibility of the first higher mode surface waves by showing that the observed first higher mode dispersion curves are matched with predicted ones calculated from *S* velocity models solely constrained by fundamental-mode dispersion curves. After the verification of the credibility of the first higher mode surface waves, we demonstrate that the inclusion of the first higher mode dispersion curves helps image deeper structures with an increase of average depths from ~0.73 to ~1.24 km, which will be beneficial to future explorations of deep oil and gas resources in the Tarim basin.

Cite this article as Xie, T., T. Xu, Y. Yang, X. Tian, J. Lin, C. Wu, and Z. Lu (2023). Observation of Higher-Mode Rayleigh Waves from Ambient Noise in the Tarim Basin, China, *Seismol. Res. Lett.* **94**, 1848–1859, doi: [10.1785/0220220361](https://doi.org/10.1785/0220220361).

[Supplemental Material](#)

Introduction

In the past two decades or so, ambient noise tomography (ANT) has been widely used to image multiscale *S*-wave velocity (V_S) of the crust and upper mantle (Sabra, Gerstoft, *et al.*, 2005; Shapiro *et al.*, 2005; Yao *et al.*, 2006; Lin *et al.*, 2008, 2013; Yang *et al.*, 2008). ANT is based on the principle that surface-wave empirical Green's functions can be reconstructed from the cross correlations of long-duration ambient seismic noise (Lobkis and Weaver, 2001; Snieder, 2004; Roux *et al.*, 2005; Sabra, Roux, and Kuperman, 2005). Because ambient seismic noise at the microseismic period band (5–20 s) mainly consists of fundamental-mode Rayleigh waves (Bonnefoy-Claudet *et al.*, 2006; Rivet *et al.*, 2015; Muir and Tsai, 2017; Chmiel *et al.*, 2019), surface waves retrieved from cross correlations of ambient noise are usually dominated by fundamental modes and previous ambient noise studies mostly performed ANT based on fundamental-mode surface waves.

In surface-wave tomography, it has been demonstrated that the inclusion of higher mode surface waves can help to better constrain V_S structure by reducing nonuniqueness in inversion and extending imaging depths of surface waves (Luo *et al.*, 2008; Tomar *et al.*, 2018; Wang *et al.*, 2019; Wu *et al.*, 2020; Ji *et al.*, 2021), as higher mode surface waves have different and

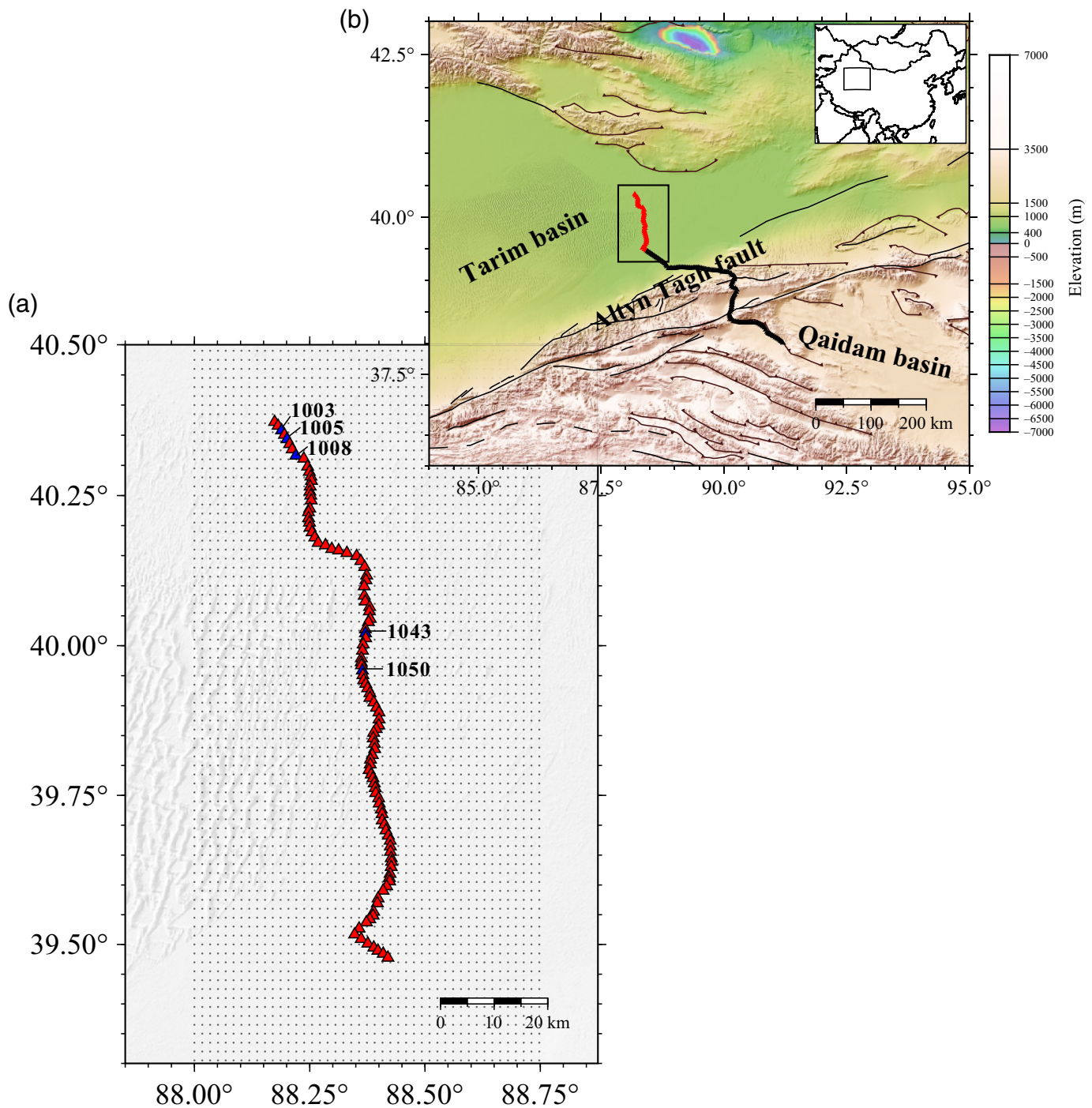
deeper sensitivities to earth structure compared to fundamental modes (Rivet *et al.*, 2015; Spica *et al.*, 2018; Tomar *et al.*, 2018; Chmiel *et al.*, 2019; Nayak and Thurber, 2020). Therefore, it is of great interest to retrieve higher mode surface waves and use them in imaging subsurface structures.

In the past few years, a few studies have been successful at retrieving higher mode surface waves from ambient noise (Nishida *et al.*, 2008; Yao *et al.*, 2011; Kimman *et al.*, 2012; Savage *et al.*, 2013; Hable *et al.*, 2019; Jiang and Denolle, 2022). In addition, almost all successful attempts of retrievals of higher mode surface waves are from arrays deployed either in ocean basins (Harmon *et al.*, 2007; Yao *et al.*, 2011; Hable *et al.*, 2019; Yang *et al.*, 2020; Yamaya *et al.*, 2021) or

1. State Key Laboratory of Lithospheric Evolution, Institute of Geology and Geophysics, Chinese Academy of Sciences, Beijing, China, <https://orcid.org/0000-0002-0370-7170> (XT); 2. University of Chinese Academy of Sciences, Beijing, China; 3. Key Laboratory of Mineral Resources, Institute of Geology and Geophysics, Chinese Academy of Sciences, Beijing, China; 4. Innovation Academy for Earth Science, CAS, Beijing, China; 5. Department of Earth and Space Sciences, Southern University of Science and Technology, Shenzhen, China, <https://orcid.org/0000-0002-1105-3824> (YY); 6. Geophysical Exploration Center, China Earthquake Administration, Zhengzhou, China; 7. Institute of Geology, Chinese Academy of Geological Sciences, Beijing, China

*Corresponding author: xutao@mail.iggcas.ac.cn

© Seismological Society of America



sedimentary basins near coastlines (Rivet *et al.*, 2015; Boué *et al.*, 2016; Ma *et al.*, 2016; Nayak and Thurber, 2020).

Because of the geometrical spreading and anelastic attenuation, the energy of higher mode surface waves contained in the short-period ambient noise generated at oceans attenuates and becomes weak when they propagate inland (Bonnetfoy-Claudet *et al.*, 2006; Yang *et al.*, 2011; Lin *et al.*, 2013; Spica *et al.*, 2018; Chmiel *et al.*, 2019). And few studies have reported that higher mode surface waves can be observed from ambient noise cross-correlation functions (CCFs) between individual station pairs in inland basins before. To retrieve higher mode surface waves in

Figure 1. (a) The location of stations (denoted by triangles) used in this study. The five stations mentioned in Figures 2, 3, 6, 8, and 9 are marked with blue triangles. The small dots represent the grid that parameterizes models in the first step of inversion in our study. (b) The whole array in our experiment. The red triangles in the black rectangle represent the stations used in this article. The thin black lines denote faults with its data taken from an open-source database called HimaTibetMap (see [Data and Resources](#); Taylor and Yin, 2009; Styron *et al.*, 2010). The inset in the top right of panel (b) shows the location of our study area, that is, the black rectangle, in a larger geographic area. The color version of this figure is available only in the electronic edition.

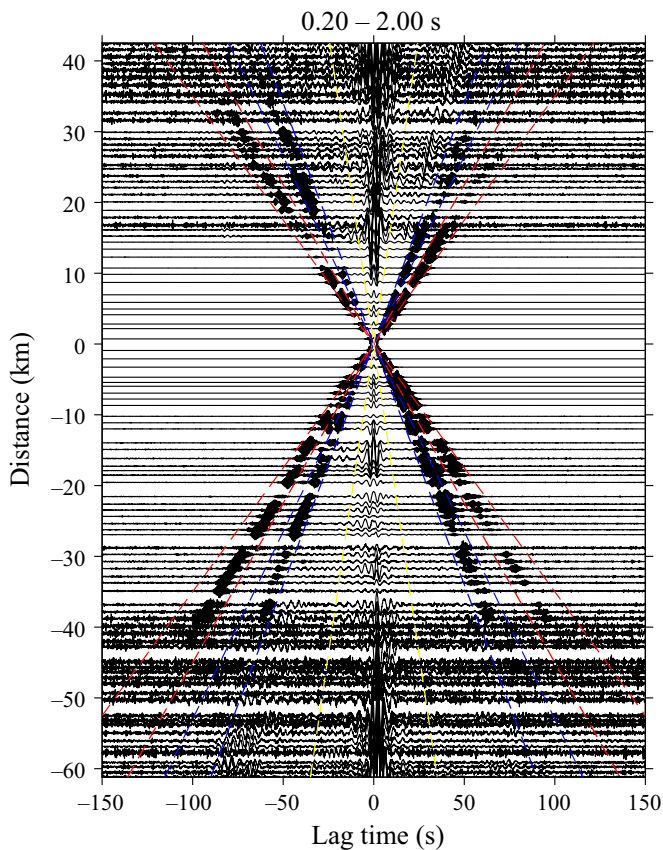


Figure 2. A cross-correlation record section centered on station 1043 in our study area. The cross-correlation functions (CCFs) are sorted by interstation distances. A negative sign of distances that represents the second station is located in the south direction relative to the station acting as the virtual source. Each CCF is band-pass filtered at a period band of 0.20–2.00 s and normalized with the maximum value of the waveform between the yellow line (with a moveout velocity of 1500 m/s) and the end of the waveform. The moveout velocities for the fundamental-mode Rayleigh waves are ~350–450 m/s (red lines) and those for the first higher mode Rayleigh waves are ~530–680 m/s (blue lines). The location of station 1043 is denoted in Figure 1. The color version of this figure is available only in the electronic edition.

inland basins, Wang *et al.* (2019) developed a dense array-based frequency–Bessel transform (F - J) method to retrieve the average higher-mode Rayleigh dispersion curves in recordings of CCFs between a large number of station pairs, and this method has been successfully applied to the U.S. Great Plains area (Wu *et al.*, 2020) to build smoothed models of velocity structures. This method has also been applied to investigate shallow crustal velocity structures, for example, a 3D V_S model of Long Beach (Fu *et al.*, 2022) and 2D V_S profile in urban areas (Li *et al.*, 2020). However, to improve the resolution of imaging using higher modes, retrievals of higher-mode surface waves and the ability to reliably measure dispersion curves between individual station pairs are important.

The Tarim basin, located in northwestern China, is the biggest inland basin in China. This basin is surrounded by several mountain ranges and plays an important role in the Cenozoic Asian orogenic system (Laborde *et al.*, 2019). Furthermore, the Tarim basin is covered by thick sediments ranging from 5 to 20 km (Li *et al.*, 2012) and is abundant in oil and natural gas resources (Kang, 2018). To the southeast, the Tarim basin is bounded by the Altyn Tagh range. We deployed a short-period dense array consisting of 483 three-component (3C) EPS-2-M6Q-C-E20 seismometers, from northwest to southeast across the southeast margin of the Tarim basin, the Altyn Tagh range, and the northern Qaidam basin (Fig. 1) to explore the fine velocity structure in upper crustal at the north margin of the Tibetan plateau. Using ambient noise data recorded by this array, we obtain ambient noise CCFs between individual station pairs.

In this study, we report the observation of both fundamental and higher mode Rayleigh waves between individual station pairs from vertical-component ambient noise CCFs. We first confirm the credibility of higher mode surface waves in CCFs between individual station pairs by showing that the observed first higher mode dispersion curves are matched with predicted ones calculated from S velocity models solely constrained by fundamental-mode dispersion curves. After that, we invert dispersion curves from the fundamental and higher mode for S -wave velocity beneath the linear station using a two-step method. Finally, we discuss the reasons for the observation of the higher mode Rayleigh waves in the Tarim basin. Our study promotes future studies of utilizing higher mode surface waves in the exploration of deep resources.

Data

The data we use for the retrieval of higher mode surface waves are from a short-period dense array deployed by the Institute of Geology and Geophysics, Chinese Academy of Sciences during a period from 17 September 2021 to 20 November 2021 (Fig. 1). The average station spacing of this array is ~1 km and the frequency range over which the amplitude response of the seismometer is flat is 100 Hz–20 s. Because only those stations located within the Tarim basin contain higher mode surface waves in our CCFs, we do not use the CCFs from stations located outside the Tarim basin.

To retrieve surface waves from ambient noise, we follow the methods of Bensen *et al.* (2007) to process ambient noise data recorded by this seismic array during the whole deployment period. We first decimate the original sampling rate from 100 to 20 Hz and cut the continuous data of vertical components into hourly segments. We then demean and detrend the hourly segments and remove their instrument responses. Furthermore, we filter the hourly segment data at a period band of 0.125–50 s. Afterward, we apply the running-absolute-mean normalization and spectral whitening to the filtered hourly segments following Bensen *et al.* (2007). After all the

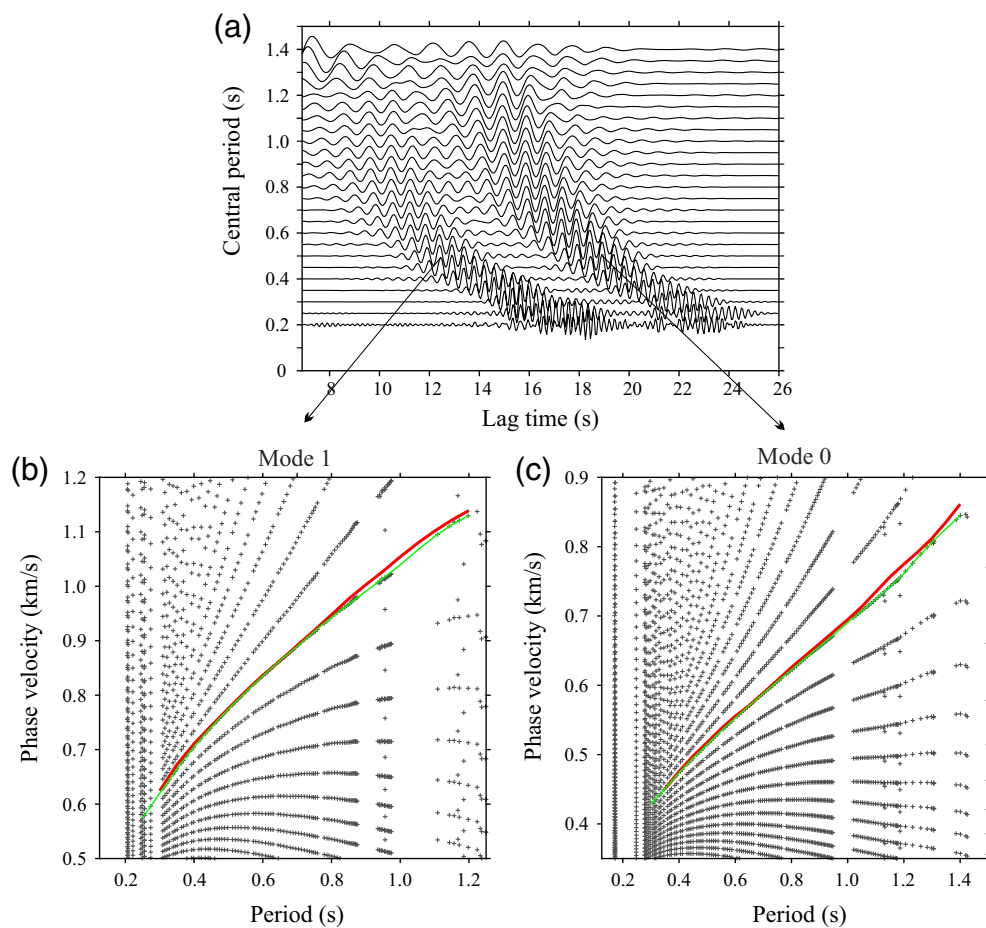


Figure 3. Extraction for phase velocity dispersion curves between an individual station pair of 1043–1050. The interstation distance of this station pair is 6.94 km. (a) A series of band-pass-filtered CCFs are sorted by the central periods ranging from 0.2 to 1.4 s with an interval of 0.05 s. (b,c) Phase velocity diagrams of (b) the first higher mode and (c) the fundamental-mode Rayleigh waves. The plus signs represent different branches of phase velocity dispersion curves resulting from the cycle ambiguity of phase of the surface waves. The red solid lines are the average phase velocity curves derived by the phase shift method for reference. The green solid lines are the phase velocity dispersion curves finally picked. The locations of stations 1043 and 1050 are shown in Figure 1. The color version of this figure is available only in the electronic edition.

preprocessing of the hourly segments, we cross correlate all hourly segments to obtain CCFs between station pairs. Finally, we adopt a phase-weighted stacking method of Li *et al.* (2017) to stack hourly CCFs to obtain final CCFs.

We band-pass filter the CCFs at several period bands (in Fig. S1, available in the supplemental material to this article, and Fig. 2) and determine that the effective period band of the Rayleigh-wave signals in CCFs is approximately 0.2–2.0 s. An example of a cross-correlation record section filtered at a period band of 0.2–2.0 s is plotted in Figure 2. Compared to most previous ambient noise studies, for which only fundamental-mode Rayleigh waves have been observed in CCFs in most situations (Yao *et al.*, 2006; Yang *et al.*, 2008), we observe two groups of wavetrains with different moveout velocities of ~350–450 and ~530–680 m/s. As Rayleigh waves are more

readily observed in most applications for ambient noise CCFs (Muir and Tsai, 2017) and we here cross correlate vertical components of noise data, we infer that the wavetrains with the smaller moveout velocity are fundamental-mode Rayleigh waves and the wavetrains with the larger moveout velocity are the first higher mode Rayleigh waves. To further investigate whether the wavetrains are indeed fundamental and first higher mode Rayleigh waves, we carry out the dispersion analysis subsequently and check whether the dispersion curves from the two waveforms are self-consistent with the notion that they are two different modes of Rayleigh waves.

Analysis of Phase Velocity Dispersion Curves

Surface waves are dispersive in layered media (Gribler *et al.*, 2016), and higher mode Rayleigh waves generally have higher phase velocities compared to the fundamental modes (Gribler *et al.*, 2016; Ma *et al.*, 2016; Gribler and Mikesell, 2019; Nayak and Thurber, 2020; Ji *et al.*, 2021). Therefore, we first measure

the phase velocities of the two groups of wavetrains to see if they possess the dispersive characteristics of surface waves.

For each CCF, we stack the positive and negative time lags of CCFs to enhance the signal-to-noise ratios (SNRs) of surface waves. We then perform a zero-phase narrowband filter on CCFs at each central period band between 0.2 and 2.0 s with a 0.05 s interval. An example of band-pass-filtered CCFs between a station pair is plotted in Figure 3a at various central periods, which demonstrates a clear dispersive feature of surface waves for both wavetrains as increasing phase velocity with periods. We adopt a modified frequency–time analysis (FTAN) method (Levshin and Ritzwoller, 2001; Bensen *et al.*, 2007; Lin *et al.*, 2008) to extract phase velocity dispersion curves of the two modes at period bands of 0.2–2.0 s. To guarantee a maximum SNR, we evaluate the phase travel time at the time of the

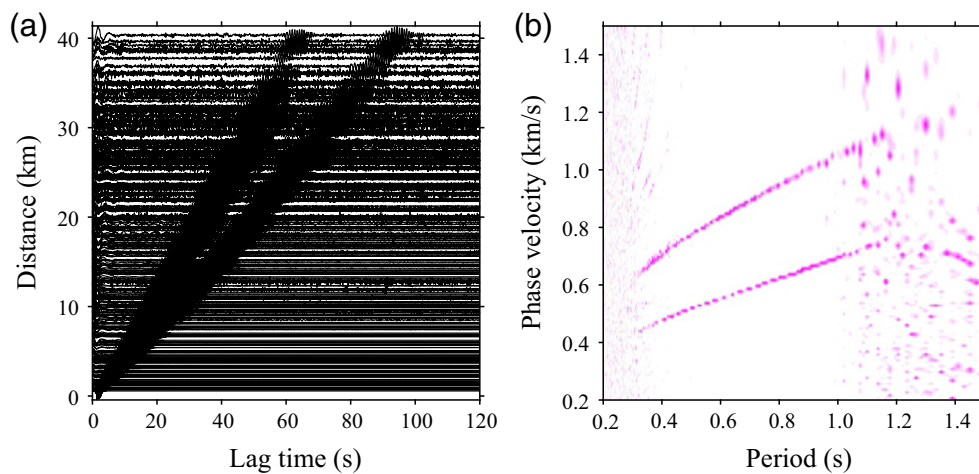


Figure 4. An example of measuring average phase velocity dispersion curves by a phase shift method at the segment interval of 40–50 km. (a) The cross-correlation record section is band-pass filtered at 0.2–2.0 s. (b) Average phase velocity dispersion curves of CCFs in panel (a) obtained by a phase shift method. Colors represent coherence values from 0 (white) to 1 (pink). The color version of this figure is available only in the electronic edition.

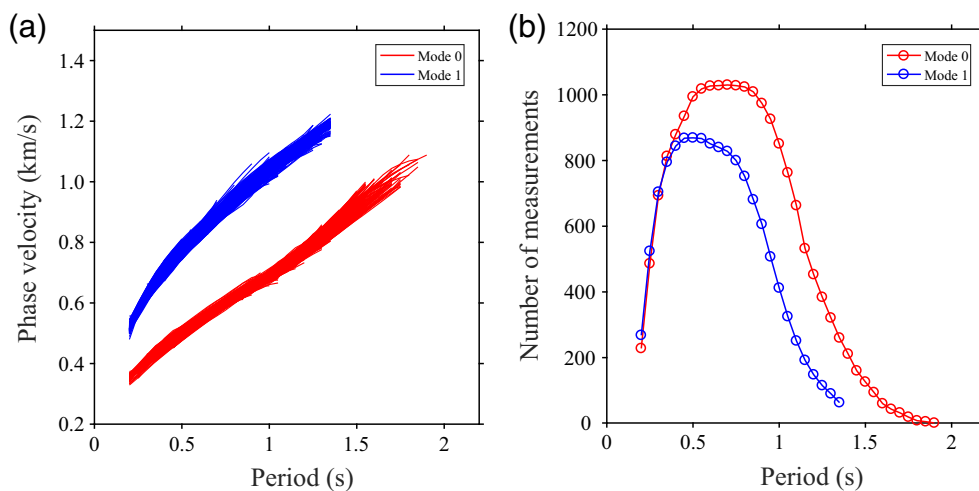


Figure 5. Phase velocity dispersion curves. (a) The phase velocity dispersion curves measured from CCFs between individual station pairs and (b) the numbers of measurements for the fundamental (in red) and the first higher mode (in blue) Rayleigh-wave dispersion curves, respectively. The color version of this figure is available only in the electronic edition.

maximum envelope peak (Aki and Richards, 2002; Lin *et al.*, 2008). As the two groups of wavetrains are separated from each other at each period, for the fundamental-mode Rayleigh waves, we first manually search the phase travel time of the maximum envelope peak in the fundamental-mode arrival time window at all periods and then calculate the phase velocities. We repeat the above process and obtain the phase velocities for the first higher mode in its arrival time window.

In our measurements of phase velocities, FTAN produces various branches of phase velocity dispersion curves resulting from the cycle ambiguity of phase of the surface waves between

station pairs as shown in Figure 3b,c. Therefore, to choose the right dispersion branch, FTAN needs a reference phase velocity dispersion curve. To find the reference dispersion curve, we adopt an array-based phase shift method of Park *et al.* (1998) to derive the reference phase velocity dispersion curve for each 10 km segment along the seismic array.

In doing so, we only choose those CCFs that contain higher mode Rayleigh waves and have interstation distances shorter than 45 km. We first sort the selected CCFs according to the distance of the midpoint of each CCF path relative to the first station on the north side of the array. We then group the CCFs into different sets with their midpoints situated in each nonoverlapped 10 km segment from the north to the south. Totally, we have 11 sets from this grouping. Using the phase shift method, we then scan phase velocities ranging from 200 to 1500 m/s with a velocity step of 10 m/s within a frequency band of 0.5–5.0 Hz with an interval of 0.01 Hz in the two main resolution spaces. One example of measuring the reference phase velocity dispersion curves at the segment interval of 40–50 km is plotted in Figure 4.

With the determination of the reference average phase velocities in each segment, we finally measure the phase velocity dispersion curves between individual station pairs. Because high-frequency surface waves become weak at long station separations due to geometrical spreading and attenuation of surface waves (Yang *et al.*, 2011; Lin *et al.*, 2013; Spica *et al.*, 2018), we measure dispersion curves of CCFs with station separations shorter than 20 km. In addition, we only retain the dispersion measurements from CCFs with an interstation distance longer than two wavelengths to satisfy the far-field approximation and with an SNR > 5 to obtain high-quality dispersion data (Xie, Xu *et al.*, 2021). The SNR here is calculated by the ratio of the

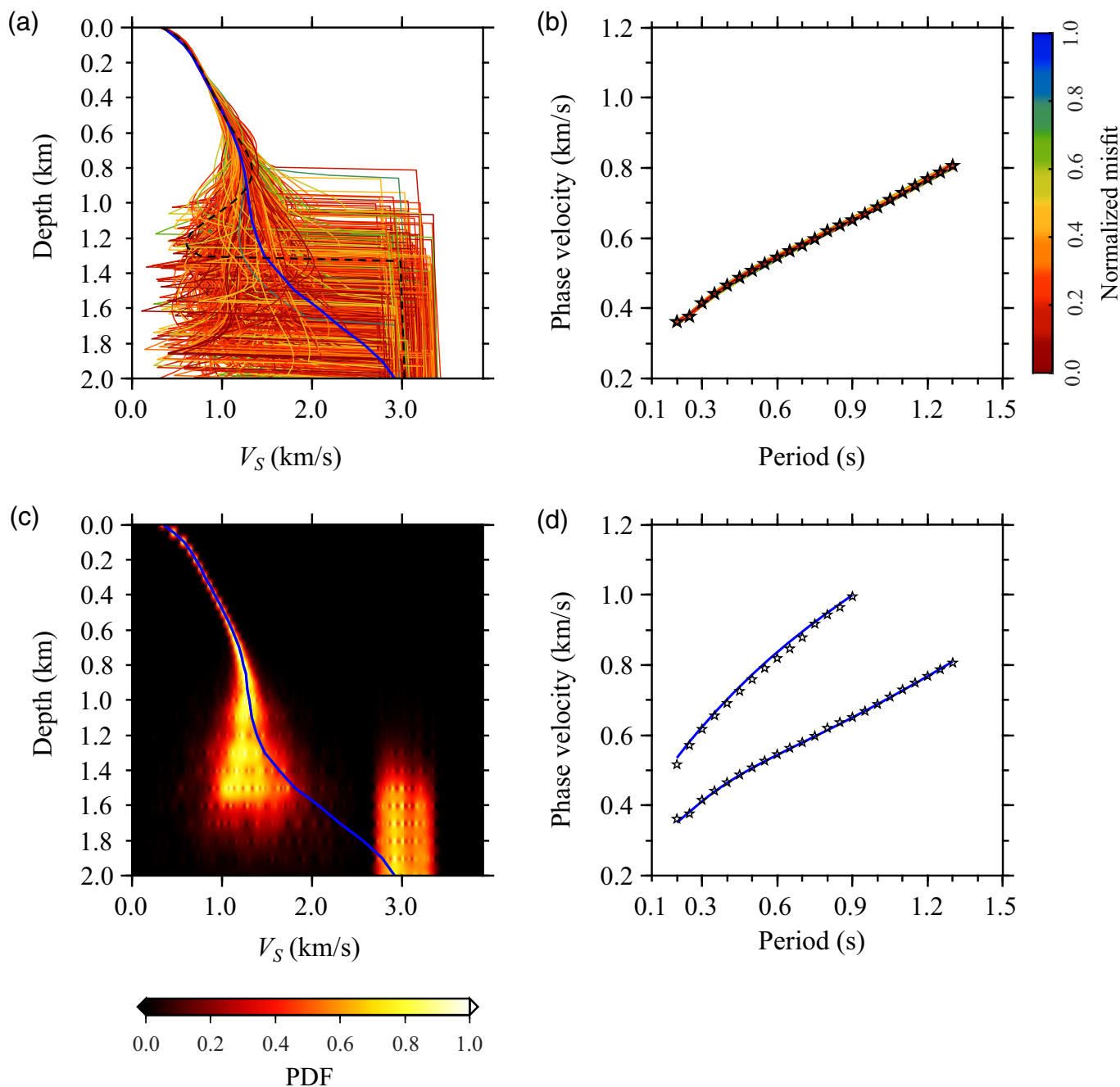


Figure 6. Verification for the credibility of first higher mode surface waves. (a) Inversion results of 1D S-wave velocity between station pair 1005–1008 by solely inverting the fundamental-mode phase velocity dispersion curves. The solid blue line is the mean of the last 1000 acceptable models (color coded by a normalized misfit), which is used for forward calculating the fundamental and the first higher mode phase velocity synthetic dispersion curves shown in panel (d). The dashed black line represents the model with the minimum normalized misfit. (b) Synthetic phase velocity dispersion curves for the last 1000

acceptable models. The observed fundamental-mode phase velocity curves are shown as black stars. (c) The normalized probability density function (PDF) constructed by the last 1000 acceptable models. The solid blue line is the mean of the last 1000 acceptable models. (d) The predicted fundamental and first higher mode phase velocity dispersion curves (solid blue lines) along with the observed ones (black stars). The locations of stations 1005 and 1008 are shown in Figure 1a. The color version of this figure is available only in the electronic edition.

maximum amplitude of surface-wave signals relative to the root mean square (rms) value within a noise window trailing the surface-wave signals in CCFs (Bensen *et al.*, 2007; Zhao *et al.*, 2020).

The final Rayleigh-wave phase velocity dispersion curves and the number of measurements for phase velocities of the two modes are shown in Figure 5. We observe the phase velocities of the two

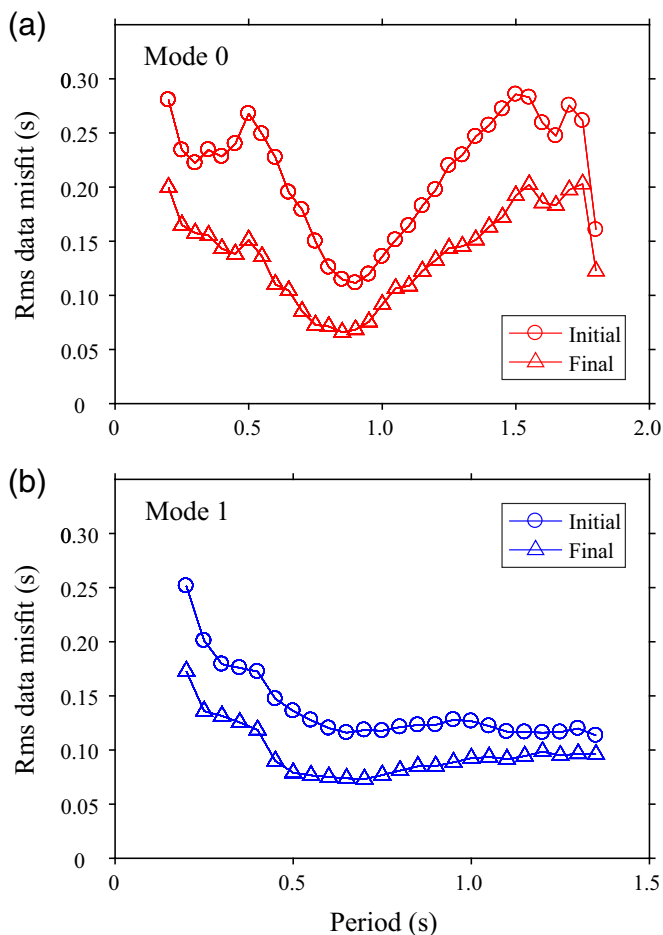


Figure 7. Reduction of root mean square (rms) data misfits for the phase travel times of (a) the fundamental and (b) the first higher mode Rayleigh waves. Note the significant reduction of misfits for the final models compared to the initial models. The color version of this figure is available only in the electronic edition.

groups of wavetrains travel with velocities of $\sim 350\text{--}1000$ and $\sim 500\text{--}1200$ m/s at a period range of 0.2–1.90 s and 0.2–1.35 s, consistent with the dispersion characteristic of surface waves and also with the notion that the first higher mode surface waves generally travel faster than the fundamental ones.

To further confirm the wavetrains with the faster propagation speeds are indeed the first higher mode surface wave, we first solely invert the fundamental-mode dispersion curves for the S-wave velocity model. Then, based on the S-wave model, we synthesize the predicted first higher mode dispersion curves. If the predicted first higher mode dispersion curves match the observed ones to a reasonable degree, we can confirm that the wavetrains with faster propagation speeds are the first higher mode surface waves. To do so, we select a station pair of 1005–1008 as an example (Fig. 6).

We adopt a Bayesian Monte Carlo method (Afonso *et al.*, 2013; Guo *et al.*, 2016) to first invert the fundamental-mode dispersion curves for the average 1D S-wave velocity between

the station pair. In this method, a Markov chain Monte Carlo (MCMC) method is adopted to search the model space with a delay rejection (DR) adaptive metropolis algorithm to sample the posterior distribution (Afonso *et al.*, 2013; Shan *et al.*, 2014; Guo *et al.*, 2016). As our study region is within the Tarim basin with a thick sedimentary coverage, in the inversion, considering the maximum period of the dispersion data, we parameterize our inversion model as a sedimentary layer with an inversion depth of up to 3 km. The S-wave velocity variations in the sedimentary layers are represented by 10 B-splines, and the search range of the S-wave velocity is from 0.1 to 2.5 km/s. We set V_P/V_S as 2 and relate ρ to V_P following the relationship of $\rho = 1.74V_P^{1/4}$ (Gardner *et al.*, 1974). The MCMC method searches S-wave velocity models within the ranges of defined velocity for a total of 320,000 times. The first 160,000 initial models are generated following the initial uniform distribution, and each model is judged twice by the DR method to determine whether it is acceptable or not. Then, all the searched 160,000 models are used as historical samples to adjust the covariance matrix of the Gaussian proposed distribution. After the first 160,000 searches, the model search goes on with the adjusted Gaussian proposed distribution and we start to record acceptable models. The probability of acceptance for each model is defined by a Metropolis law (Text S1; Yang *et al.*, 2020). Meanwhile, the Gaussian distribution is also subsequently updated by historical samples for every 40,000 searches in the last 160,000 searches. Finally, we use the last 1000 acceptable samples to construct the posterior probability density function (PDF) and take the mean of these 1000 models as the final S velocity model. The forward calculation in the search is performed by a Computer Programs in Seismology (CPS) program (Herrmann, 2013).

Based on the inverted 1D S-wave velocity model, we synthesize the predicted fundamental and the first higher mode phase velocity dispersion curves and compare the predicted fundamental and first higher mode phase velocity dispersion curves with the observed ones. As shown in Figure 6d, the synthetic fundamental and first higher mode phase velocity dispersion curves are matched with the observed ones very well, suggesting that the two groups of wavetrains are indeed the fundamental and first higher mode surface waves.

ANT of the Fundamental Modes and First Higher Modes

With the identification of the fundamental and first higher mode surface waves, we here demonstrate that the inclusion of the first higher mode dispersion curves improves the inversion for subsurface S-wave structures. We compare the results of joint inversion of the fundamental and the first higher mode phase velocities with those solely based on the fundamental-mode phase velocities.

We take a two-step method to invert interstation dispersion curves from CCFs for S-wave velocities beneath the seismic array. In the first step, we adopt a Fast-marching surface

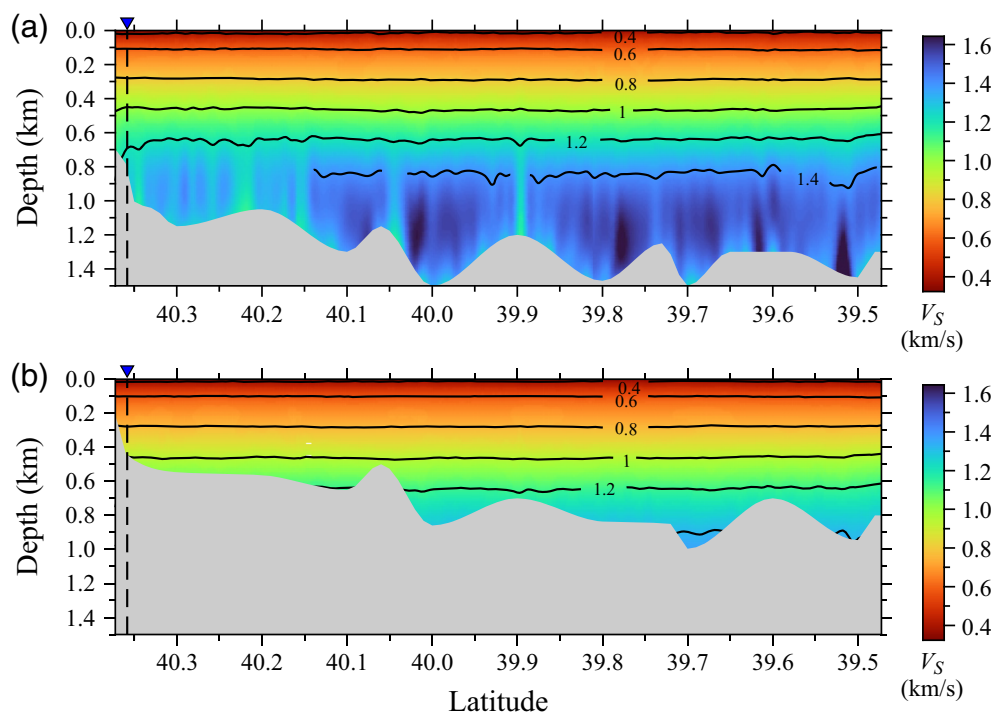


Figure 8. S-wave velocity profile (a) by jointly inverting the fundamental mode and the first higher mode Rayleigh waves and (b) by solely inverting the fundamental-mode phase velocity dispersion curves. These two profiles only plot V_S at the reliable depths above the gray-shaded area, which is defined in detail in the [ANT of the Fundamental Modes and First Higher Modes](#) section. The blue triangles show the location of station 1003. The color version of this figure is available only in the electronic edition.

tomography method (Rawlinson and Sambridge, 2005; Fang *et al.*, 2015) to obtain phase velocity maps of the fundamental and the first higher mode surface waves for the areas covered by the seismic array. To include all the possible ray paths from our seismic profile, we parameterize the initial model in our study region using a grid with a 0.015° interval in latitude and 0.017° in longitude as shown in Figure 1. In the inversion, at each period, we take the average phase velocity at this period as the background velocity for the initial model. We test different smoothing and damping regularization parameters and determine the best values based on an L -curve method, which considers the balance of rms data misfit, model roughness, and model variance (Fig. S2; Rawlinson and Sambridge, 2005; Fang *et al.*, 2015; Xie, Xu, *et al.*, 2021). Finally, we obtain phase velocity maps at a period band of 0.2–1.80 s for the fundamental mode and 0.2–1.35 s for the first higher mode. Compared to the initial models, the rms data misfits of the final models are largely reduced with an average reduction of 36.02% and 29.31% for the fundamental and the first higher mode, respectively, as shown in Figure 7, which demonstrates that the final models fit the observed data better. Then, we extract the local phase velocity dispersion curves of fundamental and the first higher mode Rayleigh waves at individual stations from the phase velocity maps.

In the second step, we invert these local phase velocity dispersion curves for 1D S-wave velocity profile beneath each station using the aforementioned Bayesian method. The final S velocity model is taken from the mean of the last 1000 acceptable models. Finally, we assemble all the 1D S-wave velocity models along the array and obtain an S-wave velocity transect. For comparison, we also solely invert the fundamental-mode local phase velocity dispersion curves for the 1D S-wave velocity profiles.

The final S-wave velocity transect along the array from the joint inversion of the fundamental and the first higher mode is plotted in Figure 8a along with the one from the inversion with the fundamental mode (Fig. 8b). For comparison, we here define a reliable depth beneath each station as the depths where

velocity variances of the last 1000 acceptable models are less than 30% relative to the final S velocity model. The gray shaded area in Figure 8 represents the depths for which constraints on the S-wave structures from the dispersion data are weak based on the definition of the aforementioned reliable depth. We can see that the inclusion of the first higher mode dispersion curves allows us to image a greater depth with an increase of average depths from ~ 0.73 to ~ 1.24 km. In addition, we also present one example of the detailed process of 1D V_S inversion beneath station 1003 in Figure 9a–f and Figure S3 (Cheng *et al.*, 2021). Beneath this station, we can see that the reliably imaged depth increases from 0.45 to 0.8 km with the inclusion of the first higher mode surface waves. We also see the nonuniqueness of shear velocity inversion is also reduced, that is, the reduction in the variances of the last 1000 accepted models. These findings are also evidenced by checking the shear-wave sensitivity kernels for the two modes, for which the first higher mode is sensitive to a deeper depth than the fundamental mode (Fig. 10; Pan *et al.*, 2019; Bai *et al.*, 2021). Furthermore, our results show that the S-wave velocities in all depths are lower than 1.6 km/s, and the velocities increase with depths and display flat-layered features, revealing the subsurface features of the Tarim basin with a sedimentary layer.

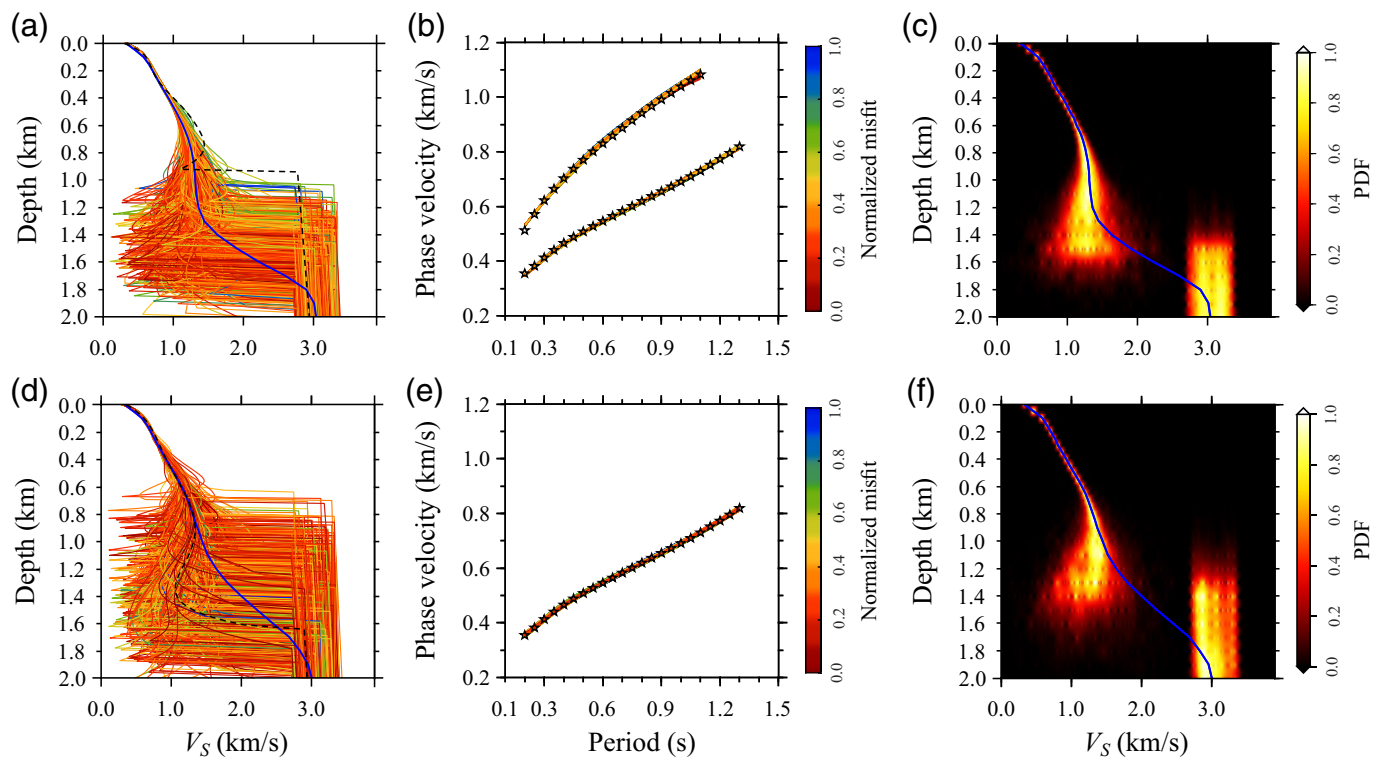


Figure 9. 1D S -wave velocity inversion results beneath station point 1003 (a) by jointly inverting the fundamental and the first mode phase velocity dispersion curves and (d) by solely inverting the fundamental-mode phase velocity dispersion curves. The final S -wave velocity models (solid blue lines) are determined by taking the average of the last 1000 acceptable models color coded by normalized misfits. The black dashed lines represent the models

with the minimum normalized misfit. (b,e) Synthetic phase velocity dispersion curves for the last 1000 acceptable models in (a,d). The observed fundamental and the first higher mode phase velocity dispersion curves are marked as black stars. (c,f) The normalized PDFs constructed by the last 1000 acceptable models. The solid blue lines are the final S -wave velocity models. The color version of this figure is available only in the electronic edition.

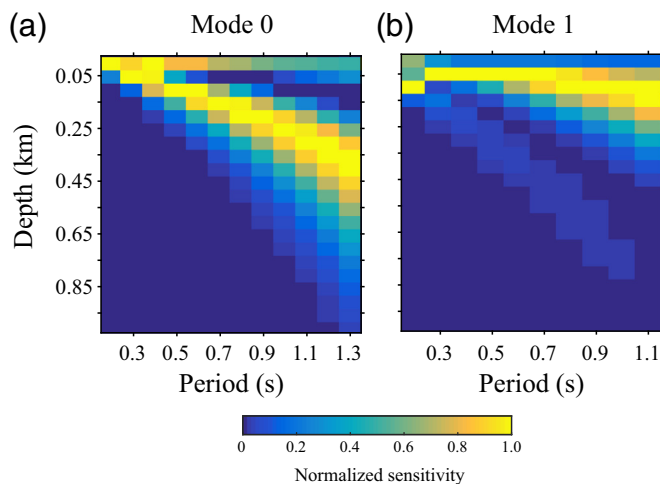


Figure 10. Sensitivity kernels plotted as variations with periods and depths for the (a) fundamental mode and (b) the first higher mode. The sensitivity kernels are calculated from the S -wave velocity model plotted in Figure 9a using the software senskernel-1.0 provided by the University of Colorado Boulder (see [Data and Resources](#)). The color version of this figure is available only in the electronic edition.

Discussions and Conclusions

We successfully observe the first higher mode Rayleigh waves and extract dispersion curves directly from CCFs between individual station pairs in an inland basin. We confirm the credibility of the observation of the first higher mode Rayleigh waves by analyzing the dispersion nature of the first higher modes. Furthermore, we show that, compared to the inversion solely with fundamental modes, the joint inversion of the fundamental and the first higher mode dispersion curves improve the constraints on the subsurface structure of sediment basins in the Tarim basin by imaging structures with a greater depth and reducing the nonuniqueness in S -wave velocity inversions.

The successful observation of the first higher mode Rayleigh waves in the Tarim basin may mainly be attributed to two factors: the generation and amplification of ambient noise (Kimman and Trampert, 2010; Boué *et al.*, 2016; Ma *et al.*, 2016; Tomar *et al.*, 2018; Nayak and Thurber, 2020; Gualtieri *et al.*, 2021; Ji *et al.*, 2021). First, considering that we do not observe higher modes in CCFs outside the Tarim basin (Fig. S4), the low-velocity sedimentary layers

at the shallow subsurface of the basin favor the excitation and amplification of the energy of higher mode surface waves. Second, the short-period bands of the higher mode Rayleigh waves in CCFs suggest that the ambient noise sources exciting the higher mode surface waves in our study area probably originate from local noise sources, such as anthropogenic noise sources from nearby cities and highways. However, limited by the configuration of the linear array in this study, we cannot locate the exact localities of the noise sources. Future works by deploying a 2D array and performing beamforming analysis are needed to investigate the origin of the noise sources.

In addition to the fundamental and first higher mode Rayleigh waves appearing in CCFs, we also observe the zero-time signals in the CCFs as shown in Figure 2. As the arrival times of these signals are nearly zero, much earlier than the arrivals of surface waves, these zero-time signals do not affect the extraction of dispersion curves of surface waves in this study. The origin of the zero-time signals is mostly body waves that propagate nearly vertically beneath this array probably coming from regional earthquakes or distant sources (Wang *et al.*, 2012; Roux *et al.*, 2016; Xie, Luo, and Yang, 2021). However, as we mention in the preceding paragraph, due to the limitation of the seismic array configuration, we cannot locate the sources of body waves either.

As is well known, the Tarim basin is abundant in deeply buried oil and gas resources, and great-depth exploration is important for achieving future exploration success in this area (Kang, 2018; Tian *et al.*, 2021; Yang *et al.*, 2021). Considering that the inclusion of the first higher mode Rayleigh waves in the inversion enables a deep imaging capability, we think there is a great potential for applications of ANT in exploring abundant oil and gas resources at great depths in the Tarim basin in the future.

Data and Resources

The phase velocity dispersion curves of fundamental and the first higher mode Rayleigh waves used in this study and the Instrument Manual (in a Chinese version) of the instrument EPS-2-M6Q-C-E20 are available from the corresponding author, xutao@mail.jggcas.ac.cn, upon request. The open-source database of HimaTibetMap was obtained from and is available at <https://github.com/HimaTibetMap/HimaTibetMap> (last accessed April 2023). The software senskernel-1.0 was obtained from the University of Colorado Boulder and is available at <https://github.com/NoiseCIEI/SensKernel> (last accessed February 2023). The supplementary material for this article includes “Text S1: Details about the Metropolis law in the MCMC method,” “Figure S1: Two more examples of cross-correlation record sections filtered at different period bands,” “Figure S2: Determination of smoothing and damping parameters,” “Figure S3: Misfits to the dispersion curves for the two modes for station 1003,” and “Figure S4: Examples of the cross-correlation functions (CCFs) located outside the Tarim basin.”

Declaration of Competing Interests

The authors declare that there are no conflicts of interest recorded.

Acknowledgments

The authors would like to thank Editor Allison Bent and two anonymous reviewers for their constructive comments. The authors acknowledge the work in the field data acquisition carried out by Geophysical Exploration Center, China Earthquake Administration. The authors appreciate the constructive discussions with Youshan Liu, Zhenbo Wu, Xiaozhou Yang, Jinyun Xie, Yanan Xie, Yingquan Sang, and Junliu Suwen. This work is financially supported by the Second Tibetan Plateau Scientific Expedition and Research Program (STEP; 2019QZKK0701), K. C. Wong Education Foundation (GJTD-2019-04) and the National Natural Science Foundation of China (Grant Numbers 42030308 and 42130807).

References

- Afonso, J., J. Fullea, W. Griffin, Y. Yang, A. Jones, J. D. Connolly, and S. O'Reilly (2013). 3-D multiobservable probabilistic inversion for the compositional and thermal structure of the lithosphere and upper mantle. I: A priori petrological information and geophysical observables, *J. Geophys. Res.* **118**, no. 5, 2586–2617.
- Aki, K., and P. G. Richards (2002). *Quantitative Seismology*, 2nd ed., University Science Books, San Francisco, California.
- Bai, T., A. Nayak, C. Thurber, X. Zeng, and M. Haney (2021). Ambient noise tomography of the Katmai volcanic area, Alaska, *J. Volcanol. Geoth. Res.* **419**, 107373, doi: [10.1016/j.jvolgeores.2021.107373](https://doi.org/10.1016/j.jvolgeores.2021.107373).
- Bensen, G. D., M. H. Ritzwoller, M. P. Barmin, A. L. Levshin, F. Lin, M. P. Moschetti, N. M. Shapiro, and Y. Yang (2007). Processing seismic ambient noise data to obtain reliable broad-band surface wave dispersion measurements, *Geophys. J. Int.* **169**, no. 3, 1239–1260.
- Bonnefoy-Claudet, S., F. Cotton, and P.-Y. Bard (2006). The nature of noise wavefield and its applications for site effects studies: A literature review, *Earth Sci. Rev.* **79**, nos. 3/4, 205–227.
- Boué, P., M. Denolle, N. Hirata, S. Nakagawa, and G. C. Beroza (2016). Beyond basin resonance: Characterizing wave propagation using a dense array and the ambient seismic field, *Geophys. J. Int.* **206**, no. 2, 1261–1272.
- Cheng, F., B. Chi, N. J. Lindsey, T. C. Dawe, and J. B. Ajo-Franklin (2021). Utilizing distributed acoustic sensing and ocean bottom fiber optic cables for submarine structural characterization, *Sci. Rep.* **11**, no. 1, 1–14.
- Chmiel, M., A. Mordret, P. Boué, F. Brenguier, T. Lecocq, R. Courbis, D. Hollis, X. Campman, R. Romijn, and W. Van der Veen (2019). Ambient noise multimode Rayleigh and Love wave tomography to determine the shear velocity structure above the Groningen gas field, *Geophys. J. Int.* **218**, no. 3, 1781–1795.
- Fang, H., H. Yao, H. Zhang, Y.-C. Huang, and R. D. van der Hilst (2015). Direct inversion of surface wave dispersion for three-dimensional shallow crustal structure based on ray tracing: Methodology and application, *Geophys. J. Int.* **201**, no. 3, 1251–1263.
- Fu, L., L. Pan, Z. Li, S. Dong, Q. Ma, and X. Chen (2022). Improved high-resolution 3D Vs model of long beach, CA: Inversion of multimodal dispersion curves from ambient noise of a dense array, *Geophys. Res. Lett.* **49**, no. 4, e2021GL097619, doi: [10.1029/2021GL097619](https://doi.org/10.1029/2021GL097619).

- Gardner, G. H. F., L. W. Gardner, and A. R. Gregory (1974). Formation velocity and density—The diagnostic basics for stratigraphic traps, *Geophysics* **39**, no. 6, 770–780.
- Gribler, G., and T. D. Mikesell (2019). Methods to isolate retrograde and prograde Rayleigh-wave signals, *Geophys. J. Int.* **219**, no. 2, 975–994.
- Gribler, G., L. M. Liberty, T. D. Mikesell, and P. Michaels (2016). Isolating retrograde and prograde Rayleigh-wave modes using a polarity mute, *Geophysics* **81**, no. 5, V379–V385.
- Gualtieri, L., E. Bachmann, F. J. Simons, and J. Tromp (2021). Generation of secondary microseism Love waves: Effects of bathymetry, 3-D structure and source seasonality, *Geophys. J. Int.* **226**, no. 1, 192–219.
- Guo, Z., Y. Yang, and Y. J. Chen (2016). Crustal radial anisotropy in Northeast China and its implications for the regional tectonic extension, *Geophys. J. Int.* **207**, no. 1, 197–208.
- Hable, S., K. Sigloch, E. Stutzmann, S. Kiselev, and G. Barruol (2019). Tomography of crust and lithosphere in the western Indian Ocean from noise cross-correlations of land and ocean bottom seismometers, *Geophys. J. Int.* **219**, no. 2, 924–944.
- Harmon, N., D. Forsyth, and S. Webb (2007). Using ambient seismic noise to determine short-period phase velocities and shallow shear velocities in young oceanic lithosphere, *Bull. Seismol. Soc. Am.* **97**, no. 6, 2009–2023.
- Herrmann, R. B. (2013). Computer programs in seismology: An evolving tool for instruction and research, *Seismol. Res. Lett.* **84**, no. 6, 1081–1088.
- Ji, Z., B. Wang, W. Yang, W. Wang, J. Su, B. Wei, H. Wang, and T. Hu (2021). Observation of higher-mode surface waves from an active source in the Hutubi Basin, Xinjiang, China, *Bull. Seismol. Soc. Am.* **111**, no. 3, 1181–1198.
- Jiang, C., and M. A. Denolle (2022). Pronounced seismic anisotropy in Kanto sedimentary basin: A case study of using dense arrays, ambient noise seismology, and multi-modal surface-wave imaging, *J. Geophys. Res.* **127**, no. 8, e2022JB024613, doi: [10.1029/2022JB024613](https://doi.org/10.1029/2022JB024613).
- Kang, Y. (2018). The resource potential and exploration for oil and gas in the Tarim Basin, *Pet. Sci. Bull.* **3**, no. 4, 369–375 (in Chinese).
- Kimman, W., X. Campman, and J. Trampert (2012). Characteristics of seismic noise: Fundamental and higher mode energy observed in the northeast of the Netherlands, *Bull. Seismol. Soc. Am.* **102**, no. 4, 1388–1399.
- Kimman, W. P., and J. Trampert (2010). Approximations in seismic interferometry and their effects on surface waves, *Geophys. J. Int.* **182**, no. 1, 461–476.
- Laborde, A., L. Barrier, M. Simoes, H. Li, T. Coudroy, J. Van der Woerd, and P. Tapponnier (2019). Cenozoic deformation of the Tarim Basin and surrounding ranges (Xinjiang, China): A regional overview, *Earth Sci. Rev.* **197**, 102891, doi: [10.1016/j.earscirev.2019.102891](https://doi.org/10.1016/j.earscirev.2019.102891).
- Levshin, A., and M. Ritzwoller (2001). Automated detection, extraction, and measurement of regional surface waves, *Pure Appl. Geophys.* **158**, no. 8, 1531–1545.
- Li, G., F. Niu, Y. Yang, and J. Xie (2017). An investigation of time-frequency domain phase-weighted stacking and its application to phase-velocity extraction from ambient noise's empirical Green's functions, *Geophys. J. Int.* **212**, no. 2, 1143–1156.
- Li, H., S. Li, X. D. Song, M. Gong, X. Li, and J. Jia (2012). Crustal and uppermost mantle velocity structure beneath northwestern China from seismic ambient noise tomography, *Geophys. J. Int.* **188**, no. 1, 131–143.
- Li, X., X. Chen, Z. Yang, B. Wang, and B. Yang (2020). Application of high-order surface waves in shallow exploration: An example of the Suzhou river, Shanghai, *Chin. J. Geophys.* **63**, no. 1, 247–255 (in Chinese).
- Lin, F.-C., D. Li, R. W. Clayton, and D. Hollis (2013). High-resolution 3D shallow crustal structure in Long Beach, California: Application of ambient noise tomography on a dense seismic array, *Geophysics* **78**, no. 4, Q45–Q56.
- Lin, F.-C., M. P. Moschetti, and M. H. Ritzwoller (2008). Surface wave tomography of the western United States from ambient seismic noise: Rayleigh and Love wave phase velocity maps, *Geophys. J. Int.* **173**, no. 1, 281–298.
- Lobkis, O. I., and R. L. Weaver (2001). On the emergence of the Green's function in the correlations of a diffuse field, *J. Acoust. Soc. Am.* **110**, no. 6, 3011–3017.
- Luo, Y., J. Xia, R. D. Miller, Y. Xu, J. Liu, and Q. Liu (2008). Rayleigh-wave dispersive energy imaging using a high-resolution linear Radon transform, *Pure Appl. Geophys.* **165**, no. 5, 903–922.
- Ma, Y., R. W. Clayton, and D. Li (2016). Higher-mode ambient-noise Rayleigh waves in sedimentary basins, *Geophys. J. Int.* **206**, no. 3, 1634–1644.
- Muir, J. B., and V. C. Tsai (2017). Rayleigh-wave H/V via noise cross correlation in southern California, *Bull. Seismol. Soc. Am.* **107**, no. 5, 2021–2027.
- Nayak, A., and C. H. Thurber (2020). Using multicomponent ambient seismic noise cross-correlations to identify higher mode Rayleigh waves and improve dispersion measurements, *Geophys. J. Int.* **222**, no. 3, 1590–1605.
- Nishida, K., H. Kawakatsu, and K. Obara (2008). Three-dimensional crustal S wave velocity structure in Japan using microseismic data recorded by Hi-net tiltmeters, *J. Geophys. Res.* **113**, no. B10, doi: [10.1029/2007JB005395](https://doi.org/10.1029/2007JB005395).
- Pan, L., X. Chen, J. Wang, Z. Yang, and D. Zhang (2019). Sensitivity analysis of dispersion curves of Rayleigh waves with fundamental and higher modes, *Geophys. J. Int.* **216**, no. 2, 1276–1303.
- Park, C. B., R. D. Miller, and J. Xia (1998). Imaging dispersion curves of surface waves on multi-channel record, *SEG Technical Program Expanded Abstracts 1998*, Society of Exploration Geophysicists, 1377–1380.
- Rawlinson, N., and M. Sambridge (2005). The fast marching method: An effective tool for tomographic imaging and tracking multiple phases in complex layered media, *Explor. Geophys.* **36**, no. 4, 341–350.
- Rivet, D., M. Campillo, F. Sanchez-Sesma, N. M. Shapiro, and S. K. Singh (2015). Identification of surface wave higher modes using a methodology based on seismic noise and coda waves, *Geophys. J. Int.* **203**, no. 2, 856–868.
- Roux, P., L. Moreau, A. Lecointre, G. Hillers, M. Campillo, Y. Ben-Zion, D. Zigone, and F. Vernon (2016). A methodological approach towards high-resolution surface wave imaging of the San Jacinto Fault Zone using ambient-noise recordings at a spatially dense array, *Geophys. J. Int.* **206**, no. 2, 980–992.
- Roux, P., K. G. Sabra, W. A. Kuperman, and A. Roux (2005). Ambient noise cross correlation in free space: Theoretical approach, *J. Acoust. Soc. Am.* **117**, no. 1, 79–84.

- Sabra, K. G., P. Gerstoft, P. Roux, W. Kuperman, and M. C. Fehler (2005). Extracting time-domain Green's function estimates from ambient seismic noise, *Geophys. Res. Lett.* **32**, no. 3, doi: [10.1029/2004GL021862](https://doi.org/10.1029/2004GL021862).
- Sabra, K. G., P. Roux, and W. Kuperman (2005). Emergence rate of the time-domain Green's function from the ambient noise cross-correlation function, *J. Acoust. Soc. Am.* **118**, no. 6, 3524–3531.
- Savage, M. K., F. C. Lin, and J. Townend (2013). Ambient noise cross-correlation observations of fundamental and higher-mode Rayleigh wave propagation governed by basement resonance, *Geophys. Res. Lett.* **40**, no. 14, 3556–3561.
- Shan, B., J. Afonso, Y. Yang, C. Grose, Y. Zheng, X. Xiong, and L. Zhou (2014). The thermochemical structure of the lithosphere and upper mantle beneath south China: Results from multiobservable probabilistic inversion, *J. Geophys. Res.* **119**, no. 11, 8417–8441.
- Shapiro, N. M., M. Campillo, L. Stehly, and M. H. Ritzwoller (2005). High-resolution surface-wave tomography from ambient seismic noise, *Science* **307**, no. 5715, 1615–1618.
- Snieder, R. (2004). Extracting the Green's function from the correlation of coda waves: A derivation based on stationary phase, *Phys. Rev. E* **69**, no. 4, 046610, doi: [10.1103/PhysRevE.69.046610](https://doi.org/10.1103/PhysRevE.69.046610).
- Spica, Z., M. Perton, N. Nakata, X. Liu, and G. C. Beroza (2018). Shallow VS imaging of the groningen area from joint inversion of multimode surface waves and H/V spectral ratios, *Seismol. Res. Lett.* **89**, no. 5, 1720–1729.
- Styron, R., M. Taylor, and K. Okoronkwo (2010). Database of active structures from the Indo-Asian collision, *Eos Trans. AGU* **91**, no. 20, 181–182.
- Taylor, M., and A. Yin (2009). Active structures of the Himalayan-Tibetan orogen and their relationships to earthquake distribution, contemporary strain field, and Cenozoic volcanism, *Geosphere* **5**, no. 3, 199–214.
- Tian, J., Q. Wang, H. Yang, and Y. Li (2021). Petroleum exploration history and enlightenment in Tarim Basin, *Xinjiang Pet. Geol.* **42**, no. 3, 272 (in Chinese).
- Tomar, G., E. Stutzmann, A. Mordret, J.-P. Montagner, S. C. Singh, and N. M. Shapiro (2018). Joint inversion of the first overtone and fundamental mode for deep imaging at the Valhall oil field using ambient noise, *Geophys. J. Int.* **214**, no. 1, 122–132.
- Wang, J., G. Wu, and X. Chen (2019). Frequency-Bessel transform method for effective imaging of higher-mode rayleigh dispersion curves from ambient seismic noise data, *J. Geophys. Res.* **124**, no. 4, 3708–3723.
- Wang, W.-T., S.-D. Ni, and B.-S. Wang (2012). Studies on a persistent localized microseism source that produces precursors on noise correlation function observed using stations in central-eastern China, *Chin. J. Geophys.* **55**, no. 2, 503–512 (in Chinese).
- Wu, G.-X., L. Pan, J.-N. Wang, and X. Chen (2020). Shear velocity inversion using multimodal dispersion curves from ambient seismic noise data of usarray transportable array, *J. Geophys. Res.* **125**, no. 1, e2019JB018213, doi: [10.1029/2019JB018213](https://doi.org/10.1029/2019JB018213).
- Xie, J., Y. Luo, and Y. Yang (2021). Retrieving PmP travel times from a persistent localized microseismic source, *Geophys. Res. Lett.* **48**, no. 21, e2021GL094827, doi: [10.1029/2021GL094827](https://doi.org/10.1029/2021GL094827).
- Xie, T., T. Xu, Y. Ai, Q. Zeng, W. Zhang, and F. Zheng (2021). Imaging the shallow crustal velocity structure of the Qingchengzi ore field on the Liaodong Peninsula, China, with a short-period dense array using ambient noise tomography, *Tectonophysics* **813**, 228913, doi: [10.1016/j.tecto.2021.228913](https://doi.org/10.1016/j.tecto.2021.228913).
- Yamaya, L., K. Mochizuki, T. Akuhara, and K. Nishida (2021). Sedimentary structure derived from multi-mode ambient noise tomography with dense OBS network at the Japan trench, *J. Geophys. Res.* **126**, no. 6, e2021JB021789, doi: [10.1029/2021JB021789](https://doi.org/10.1029/2021JB021789).
- Yang, X., Y. Luo, H. Xu, and K. Zhao (2020). Shear wave velocity and radial anisotropy structures beneath the central Pacific from surface wave analysis of OBS records, *Earth Planet. Sci. Lett.* **534**, 116086, doi: [10.1016/j.epsl.2020.116086](https://doi.org/10.1016/j.epsl.2020.116086).
- Yang, X., J. Tian, Q. Wang, Y. Li, H. Yang, Y. Li, Y. Tang, W. Yuan, and S. Huang (2021). Geological understanding and favorable exploration fields of ultra-deep formations in Tarim Basin, *China Pet. Explor.* **26**, no. 4, 17 (in Chinese).
- Yang, Y., M. H. Ritzwoller, and C. H. Jones (2011). Crustal structure determined from ambient noise tomography near the magmatic centers of the Coso region, southeastern California, *Geochem. Geophys. Geosys.* **12**, no. 2, doi: [10.1029/2010GC003362](https://doi.org/10.1029/2010GC003362).
- Yang, Y., M. H. Ritzwoller, F.-C. Lin, M. P. Moschetti, and N. M. Shapiro (2008). Structure of the crust and uppermost mantle beneath the western United States revealed by ambient noise and earthquake tomography, *J. Geophys. Res.* **113**, no. B12, doi: [10.1029/2008JB005833](https://doi.org/10.1029/2008JB005833).
- Yao, H., P. Gouédard, J. A. Collins, J. J. McGuire, and R. D. van der Hilst (2011). Structure of young East Pacific Rise lithosphere from ambient noise correlation analysis of fundamental- and higher-mode Scholte-Rayleigh waves, *C. R. Geosci.* **343**, no. 8, 571–583.
- Yao, H., R. D. van Der Hilst, and M. V. De Hoop (2006). Surface-wave array tomography in SE Tibet from ambient seismic noise and two-station analysis—I. Phase velocity maps, *Geophys. J. Int.* **166**, no. 2, 732–744.
- Zhao, K., Y. Yang, and Y. Luo (2020). Broadband finite frequency ambient noise tomography: A case study in the western united states using USArray stations, *J. Geophys. Res.* **125**, no. 6, e2019JB019314, doi: [10.1029/2019JB019314](https://doi.org/10.1029/2019JB019314).

Manuscript received 16 November 2022

Published online 1 May 2023